Non-specular reflection of a narrow spatially phase-modulated Gaussian beam

Yuliya S. Dadoenkova,[1] Igor A. Glukhov,[1,2] Sergey G. Moiseev,[2,3] and Florian F. L. Bentivegna[1,*]

[1]*Laboratoire des Sciences et Techniques de l'Information, de la Communication et de la Connaissance (Lab-STICC, UMR 6285), CNRS, École Nationale d'Ingénieurs de Brest, 29238 Brest Cedex 3, France*
[2]*Ulyanovsk State University, Leo Tolstoy Str. 42, 432970 Ulyanovsk, Russia*
[3]*Kotelnikov Institute of Radio Engineering and Electronics of the Russian Academy of Sciences, Ulyanovsk Branch, Goncharov Str. 48/2, 432071 Ulyanovsk, Russia*
*Corresponding author: fb@enib.fr

The lateral and angular Goos–Hänchen shifts undergone upon reflection on a dielectric plate by a spatially phase-modulated Gaussian beam are derived. It is shown that the amplitude and direction of both lateral and angular shifts are very sensitive to the degree of spatial phase modulation of the incident beam, so that such modulation thus provides a means to control those shifts. It is also shown that the modulation incurs some beam reshaping upon reflection. Analytical calculations of the lateral shift are found to be in good agreement with numerical simulations of beam propagation before and after reflection. In these simulations, the required spatial transverse phase modulation is achieved by focusing a microwave Gaussian beam onto the dielectric plate with a non-spherical lens or a flat-surfaced thin lamella exhibiting a suitable gradient of its refractive index. The optimal parameters governing the spatial phase modulation are discussed to achieve: (i) enhancement of the lateral shift of a spatially phase-modulated beam in comparison to that of a non-modulated beam and (ii) simultaneous large values of reflectivity and of the lateral shift, while keeping the reshaping of the reflected beam to a minimum.   © 2022 Optica Publishing Group

1. INTRODUCTION

Non-specular effects occurring upon the reflection of light wave packets from various optical structures have been intensively studied in the last two decades. These effects include both lateral and transverse shifts of reflected beams relative to the position predicted by ray optics [first described, in the context of total internal reflection, as Goos–Hänchen (GH) [1] and Imbert–Fedorov [2,3] effects, respectively] [4], as well as the corresponding angular shifts in the plane of incidence or perpendicular to it, i.e., deviations of the reflection angle from the value it takes in the frame of geometric optics [5,6].

Although these effects are, as a rule, rather small, the beam shifts have nevertheless been reported to take potentially significant values in many configurations, including upon total internal reflection [1,7], but also at the vicinity of minima of the reflection coefficient, for instance, at Brewster and pseudo-Brewster incidence angles [8–10], near the edges of photonic bandgaps in photonic crystals [11], or in a nanophotonic cavity [12]. In all cases, measurements of the beam shifts can be made using conventional methods based on position sensitive detectors, while a charge-coupled device can give more detailed information about the profile of the reflected beam [13]. More

precise detection techniques include interferometric setups [14,15] or signal enhancement techniques [7,10,16–19].

Far from being mere curiosities, such beam shifts can obviously be exploited to yield information about the material(s) constituting the optical structure from which reflection takes place or about the medium surrounding that structure. Indeed, as they can be shown to be extremely sensitive to tiny variations of material properties (in particular, permittivity) upon any kind of external excitations (electric or magnetic fields, pressure, temperature, mechanical strain, etc.), these effects are good candidates for the design of very precise sensors in particular, which is one of the main reasons they have attracted much attention lately. Indeed, lateral shifts can be put to use for the design of bio- or chemical sensors [20,21] and surface plasmon resonance sensors [22] or simply for precise measurement of refractive indices [23]. In some systems, the dependence of the GH shift on temperature can be used for the design of thermal sensors [24,25]. Beyond sensing applications, the principles of optical switches [26], beam splitters [27], and de/multiplexers [28] and monitoring of local electric and magnetic fields [29] or optical differential operation and image edge detection [30] have been proposed on the basis of the GH effect.

To that intent, however, it is also desirable to be able to enhance and, particularly, control in a reversible way the beam shifts, as well as relate the values they assume with the changes of permittivity of the materials the light beam encounters. The control of GH beam shifts has been studied in a variety of functional materials and structures. For instance, an external magnetic field can tune the GH shift in magnetic media [17,31–36]. Similarly, in combined magneto-optic and electro-optic systems, the shift can be controlled via external electric or magnetic fields [24,31,37,38]. A GH shift can be induced through the electro-optic effect [39] or by misfit strain [8].

In all these instances, the focus has for the most part been set on ways to design the optical system in which beam shifts take place, as well as to select the properties of its constituents, to achieve the desired control and enhancement of the effect and possibly use it for applications. More rarely has the focus been set on the properties of the beam itself, specifically on the way it can be tailored for an enhanced control of the GH effect, but also on the way the reflected beam can be distorted as a corollary to that effect. Among those rarer studies, let us note the demonstration that the lateral GH shift of light beams reflected and transmitted through a layered dielectric structure can be effectively controlled by focusing (and defocusing) the incident beam [40], with an increase of the shift when the beam is narrower. A significant reshaping of the reflected light beam has been discussed in a number of studies [41–44], including the observation that it can even split into two beams when a giant shift occurs [45]. In multilayered structures, reshaping takes place due to the interference between waves reflected from all interfaces [46]. As a rule, beam distortion is also more noticeable for narrow beams with waists of the same order of magnitude as their wavelength. Thus, reshaping the beam upon reflection requires additional studies.

In this paper, we discuss one such alternative method of exaltation of the lateral beam shift related not to specific properties of the structure it interacts with, but to the properties of the beam itself. Specifically, we present analytical and numerical calculations to investigate the effect of a *transverse spatial modulation of the phase* of a narrow Gaussian beam on lateral and angular shifts, as well as the reshaping it undergoes in its plane of incidence upon reflection off a simple dielectric isotropic plate. Those calculations were carried out in the microwave domain. The paper is organized as follows. In Section 2, we provide an analytical derivation of the reflected microwave electric field at the upper surface of the plate. In Section 3, we show how it can be used for calculation of the lateral beam shift for various degrees of phase modulation of the incoming wave packet. In Section 4, we show the results of the numerical simulations of beam propagation before and after reflection from the plate and discuss the influence of the spatial phase modulation of the Gaussian beam on its lateral and angular shifts, as well as its reshaping upon reflection. The conclusions of our study (Section 5) are followed with Appendix A, which describes ways to achieve the desired phase modulation of the incoming Gaussian beam.

2. GEOMETRY AND ANALYTICAL DESCRIPTION

In this study, we consider the reflection of a microwave Gaussian beam from a simple, homogeneous, isotropic, dielectric, non-magnetic plate of refractive index n_P and thickness d, as shown in Fig. 1. The refractive index of the surrounding medium is n_S. The upper and lower surfaces of the plate are parallel to the (xy) plane of a Cartesian system of coordinates.

A two-dimensional (2D) monochromatic Gaussian s-polarized beam (wavelength λ_0 in vacuum and angular frequency $\omega = 2\pi c/\lambda_0$) impinges on the top surface of the plate. The propagation direction of the beam is determined by its central wave vector $\mathbf{k}_c$, with $k_c = k_0 n_S$, where $k_0 = 2\pi/\lambda_0$ is the wavenumber of the beam in vacuum. The incidence angle θ is defined as the angle between $\mathbf{k}_c$ and the normal to the surface parallel to the z axis. In the (xz) plane of incidence, a system of x' and z' axes (obtained through a rotation of the x and z axes by an angle θ around the y axis) is associated to the beam, so that its central wave vector is parallel to the z' axis. The lateral dimensions of the plate, along the x and y axes, are supposed to be much larger than the diameter of the Gaussian beam, so that side effects can be neglected. The choice of a 2D beam description in which the electric field profile does not depend on the y coordinate in the direction perpendicular to the plane of incidence [see Eq. (1)] is justified by the fact that this study is devoted to the non-specular effects (in particular, beam shifts) that can be observed in that plane. Indeed, upon reflection, a Gaussian beam undergoes a GH lateral shift Δx in its plane of incidence (Fig. 1) that can be seen as a translation of the central wave vector of the reflected beam (solid red arrow) with respect to the direction of specular reflection (dashed red arrow).

In this paper, we specifically study the effect of a spatial modulation of the phase of the incident Gaussian beam on the lateral (as well as angular) shift and the simultaneous reshaping of the reflected beam. This modulation is quantified by the additional (in comparison with the expression of the field for a usual Gaussian beam) complex exponential factor that depends on the
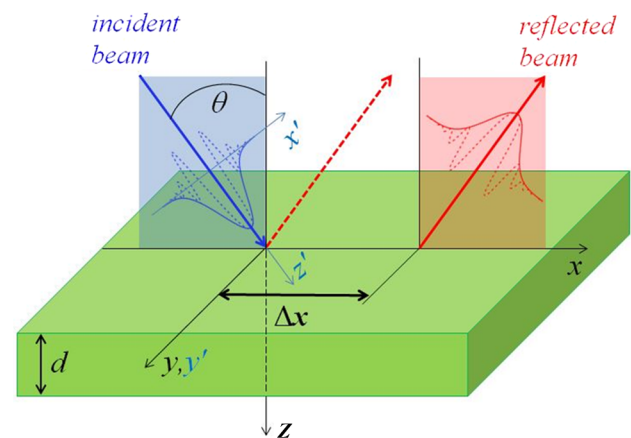

Fig. 1. Schematic of the system. A 2D Gaussian microwave beam impinges on the upper surface of a dielectric plate of thickness d. The incidence plane is (xz), and θ is the incidence angle. The lateral shift of the reflected beam is denoted Δx. Solid and dashed curves respectively show the profiles of the modulus and real part of the optical electric fields of the incident (blue curves) and reflected (red curves) beams. The dashed red arrow shows the direction of specular reflection without lateral shift.

real-valued coefficient ξ in the following expression of the transverse electric field amplitude distribution $E_y^{(i)}(x', z')$, in which the origin common to the (xyz) and $(x'y'z')$ Cartesian systems of axes coincides with the center of the incident 2D Gaussian beam in the plane of its waist, and the time dependence of the propagating wave packet is chosen as $\exp(i\omega t)$:

$$E_y^{(i)}(x', z') = E_0 \sqrt{\frac{w_0}{w(z')}} \exp\left[-\left(\frac{1}{w^2(z')} + i\frac{\xi}{w_0^2} \right) x'^2 \right]$$

$$\times \exp\left[i\eta(z') - ik_c \left(z' + \frac{x'^2}{2R(z')} \right) \right]. \tag{1}$$

In Eq. (1), z' is the algebraic axial distance from the waist, $w(z')$ is the beam radius (defined as the distance from the z' axis for which the field amplitude falls to $1/e$ of its axial value), $w_0 = w(0)$ is the waist radius, and E_0 is the axial value of the field amplitude at the waist. An important characteristic parameter of the Gaussian beam is its Rayleigh length $z'_R = k_0 w_0^2/2$, from which the z'-dependent beam parameters in Eq. (1) can be deduced, namely, the beam radius at position z',

$$w(z') = w_0 \sqrt{1 + \left(\frac{z'}{z'_R} \right)^2}, \tag{2}$$

the radius of the wavefront curvature at position z',

$$R(z') = \frac{z'^2 + z'^2_R}{z'}, \tag{3}$$

and its Gouy phase

$$\eta(z') = \arctan\left(\frac{z'}{z'_R} \right). \tag{4}$$

It should be noted that although similar at first glance, phase factors $\exp\{-i\xi x'^2/w_0^2\}$ and $\exp\{-ik_c x'^2/2R(z')\}$ in Eq. (1) are not equivalent, since the latter varies with the position z' along the propagation axis of the incident beam and explicitly depends on the curvature radius of the wavefront, especially at large distances from the beam waist, and thus does not yield a parabolic modulation of the phase. It is also worth noting that the additional imaginary factor $-i\xi x'^2/w_0^2$ in the spatial dependence of the field profile of a Gaussian beam is analogous to a similar term describing linearly chirped Gaussian pulses in the time/frequency domain [47,48]. The phase modulation parameter ξ is thus the spatial equivalent of the linear chirp parameter of such a pulse.

With the choice of origin for both systems of axes mentioned above, the center line of the Gaussian incident beam crosses the upper surface of the plate at the point $\{x = x' = 0, y = y' = 0, z = z' = 0\}$, and the center of the beam in the waist plane thus coincides with $z' = 0$ on that surface. In oblique incidence (for $\theta \neq 0$), the other points of the beam waist are located above or below the upper surface of the dielectric plate. Using Eq. (1) and the relations

$$x' = x\cos\theta, \quad z' = x\sin\theta, \tag{5}$$

the complex amplitude of the incident electric field on the upper surface of the plate ($z = 0$) in the (x, y, z) system of coordinates is

$$E_y^{(i)}(x, z=0) = E_0 \sqrt{\frac{w_0}{w(x)}} \exp\left[-\left(\frac{1}{w^2(x)} + i\frac{\xi}{w_0^2} \right) x^2 \cos^2\theta \right]$$

$$\times \exp\left[i\eta(x) - ik_c \left(x\sin\theta + \frac{1}{2R(x)} x^2 \cos^2\theta \right) \right], \tag{6}$$

where $w(x)$, $R(x)$, and $\eta(x)$ are thus calculated for $x = z'/\sin\theta$.

In the paraxial approximation, in the vicinity of the beam waist (i.e., when $z' \ll z'_R$), one can see from Eqs. (2)–(4) that $w(z') \approx w_0$, $R(z') \to \infty$, and $\eta(z') \approx 0$ for all points inside the beam spot at the upper surface of the plate (i.e., for $z = 0$). Thus, the electric field distribution of the incident beam on that surface can be written as

$$E_y^{(i)}(x, z=0) = E_G^{(i)}(x) \exp\left(-ik_{cx} x \right), \tag{7a}$$

with

$$E_G^{(i)}(x) = E_0 \exp\left[-\frac{(1 + i\xi)x^2\cos^2\theta}{w_0^2} \right], \tag{7b}$$

and where $k_{cx} = k_c \sin\theta$ is the x component of the central wave vector of the incident beam in the surrounding medium.

The spatial profile $E_y^{(r)}(x)$ of the reflected beam at the upper surface of the plate can then be obtained using the inverse spatial Fourier transform [8,24]:

$$E_y^{(r)}(x) = \frac{1}{\sqrt{\pi}} \int_{-\infty}^{\infty} E_y^{(i)}(K)\Re(K + k_{cx}) \exp(iKx)dK, \tag{8}$$

where

$$E_y^{(i)}(K) = \int_{-\infty}^{\infty} E_y^{(i)}(x) \exp(-iKx)dx$$

$$= E_0\sqrt{\pi} \sqrt{\frac{w_0^2}{(1 + i\xi)\cos^2\theta}} \exp\left[-\frac{1}{4} \frac{w_0^2 K^2}{(1 + i\xi)\cos^2\theta} \right] \tag{9}$$

is the incident field distribution in the spatial frequency domain. In Eqs. (8) and (9), the spatial Fourier variable K is defined as $K = k_x - k_{cx}$, where k_x is the x component of the wave vector $\mathbf{k}$ of any given spatial Fourier component of the incoming field distribution $E_y^{(i)}(x)$, and the corresponding $\Re(K + k_{cx}) = \Re(k_x)$ is the complex reflection coefficient of the system at a given position x across the beam at the surface of the plate. This reflection coefficient $\Re$ is deduced from Maxwell's equations and from the boundary conditions at each interface in the system as [49]

$$\Re(k_x) = \frac{r\left[1 - \exp(2ik_{tz}d) \right]}{1 - r^2 \exp(2ik_{tz}d)}, \quad \text{with } r = \frac{k_z - k_{tz}}{k_z + k_{tz}}, \tag{10}$$

where, for any given spatial Fourier component of the incoming field distribution, $k_z = k_0 n_S \cos\theta'$ and $k_{tz} = k_0 n_P \cos\theta'_t$ are the components along the z axis of its wave vector $\mathbf{k}$ and of its corresponding refracted wave vector $\mathbf{k}_t$, respectively. Angles θ' and θ'_t are thus the incidence angle and refraction angle in the plate respectively associated to $\mathbf{k}$ and $\mathbf{k}_t$ and they are related by Snell's law $n_S \sin\theta' = n_P \sin\theta'_t$. The spread of values assumed

by angles θ' and θ'_t reflects the divergence of the incoming Gaussian beam. Equations (8)–(10) lead to determination of the reflected beam intensity profile from which, after comparison with the incoming beam intensity profile, the value of the lateral shift at the upper surface of the plate, denoted Δx, can be numerically deduced. As a rule, an angular shift $\Delta\theta$ with respect to the specular geometry can also be observed. Its value cannot be deduced from the analytical approach described above and discussed in Section 3 (as that approach yields the field distribution at the surface of the plate only), but it can be obtained from numerical simulations of the propagation of the Gaussian beam after reflection (see Section 4).

3. ANALYTICAL STUDY OF THE EFFECT OF PHASE MODULATION ON THE REFLECTED BEAM AT THE SURFACE OF THE PLATE

In this section, we apply the previous analytical description to a Gaussian beam in the microwave domain, for which the lateral and angular beam shifts are expected to reach large and easily measurable values. Note that the intermediate Fourier transforms expressed in Eqs. (8) and (9) require numerical calculations.

Our simulations were carried out for a dielectric plate made of fused quartz (relative permittivity $\varepsilon_P = n_P^2 = 3.8$ at vacuum wavelength $\lambda_0 = 2.912$ mm [44] and thickness $d = 8.33$ mm) surrounded by air ($n_S = 1$). For that value of thickness d, the reflection coefficient $\mathfrak{R}$ deduced from Eq. (10) can be shown to reach a zero minimum at an incidence angle of approximately 18.5°. Around that incidence angle, for small but non-zero values of $\mathfrak{R}$, beam shifts are known to reach large values [9]. The waist of the incident Gaussian beam is chosen as $w_0 = 3\lambda_0$. In this case, the Rayleigh length is $z'_R \approx 84.5$ mm, so that we can neglect the variations in beam diameter across the thickness of the plate.

The transverse spatial distribution of the normalized Gaussian amplitude $E_G^{(i)}(x)/E_0$ of the electromagnetic field at the upper surface of the plate ($z = 0$) is shown in Fig. 2 as a function of the incidence angle and for the spatial modulation parameter $\xi = -5$. Figs. 2(a)–2(c) present the modulus $|E_G^{(i)}/E_0|$, real part Re $[E_G^{(i)}/E_0]$, and imaginary part Im $[E_G^{(i)}/E_0]$ of the normalized amplitude, respectively, and Fig. 2(d) shows the cross sections of distributions in (a)–(c) for an incidence angle $\theta = 20°$. As expected from Eq. (7b), the distribution of the Gaussian field amplitude is symmetrical with

respect to the x axis (position $x = 0$ corresponds to the center of the incident beam waist). Although the phase modulation of the Gaussian beam (for $\xi \neq 0$) does not affect the envelope (modulus) of the field amplitude, it does modify the real and imaginary parts of $E_G^{(i)}(x)$, and an increase of the modulation parameter ξ leads to increasingly fast oscillations of Re $[E_G^{(i)}/E_0]$ and Im $[E_G^{(i)}/E_0]$ along the x axis. In accordance with Eq. (7b), a reversal of the sign of ξ reverses the sign of the imaginary part of the Gaussian field amplitude. As a whole, the phase modulation of the field can be expected to exert a noticeable influence on the overall reflected beam, as the latter results from the interference between multiple waves reflected from the upper and lower surfaces of the dielectric plate.

This is clearly illustrated in Fig. 3, where the transverse distribution along the x axis of the normalized modulus $|E^{(r)}/E_0|$ of the reflected field at the upper surface of the plate ($z = 0$), deduced from Eqs. (1)–(10), is shown as a function of incidence angle θ and for different values of the spatial modulation parameter ξ. The black curves follow the position of maximum beam intensity, i.e., a departure of those lines from $x = 0$ indicates and quantifies the lateral beam shift Δx. In the absence of spatial modulation [$\xi = 0$, Fig. 3(a)], the reflected beam already exhibits significant distortion, with respect to the Gaussian profile of the incident beam, in particular, in the vicinity of incidence angles corresponding to minima of the modulus of reflection coefficient $\mathfrak{R}$— specifically, around $\theta = 18.5°$ and $\theta = 60°$ [the precise values of those angles are determined using Eq. (10)]. Indeed, near $\theta = 18.5°$, the reflected wave splits into two beams with almost equal maxima. With an increase of the absolute value of the spatial phase modulation parameter ξ [Figs. 3(b)–3(g)], the distortion of the reflected field becomes stronger, and larger intervals of θ appear for which the profile of the reflected field is split and exhibits two peaks. Due to this beam reshaping, the determination of the lateral shift, as calculated analytically at the surface of the plate, is sometimes ambiguous, since both maxima of the split beam can be of comparable amplitudes—this is especially true in the case of a non-modulated beam, as evidenced by the black lines in Fig. 3.

This ambiguity, however, is less of a difficulty for incidence angles far from those for which $|\mathfrak{R}|$ nears a minimum. In this case, the reflected field is still split in two, but one maximum is visibly larger than the other one [see, for example, Figs. 3(e)–3(g), as well as the discussion of Fig. 4 in the next section], and for all intents and purposes, the lateral beam shift Δx can be defined as the shift in position of the brighter part of the
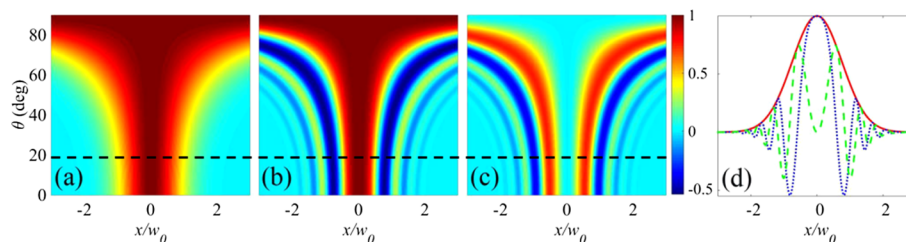

Fig. 2. Normalized distribution of the amplitude of the incident spatially modulated Gaussian beam at the upper surface of the plate (at $z = 0$) as a function of the incidence angle and for spatial modulation parameter $\xi = -5$. (a) modulus $|E_G^{(i)}/E_0|$, (b) real part Re $[E_G^{(i)}/E_0]$, and (c) imaginary part Im $[E_G^{(i)}/E_0]$. (d) Cross sections of (a)–(c) for incidence angle $\theta = 20°$ (horizontal black dashed lines), where the red solid, blue dotted, and green dashed curves denote the modulus and real and imaginary parts of the normalized field, respectively.
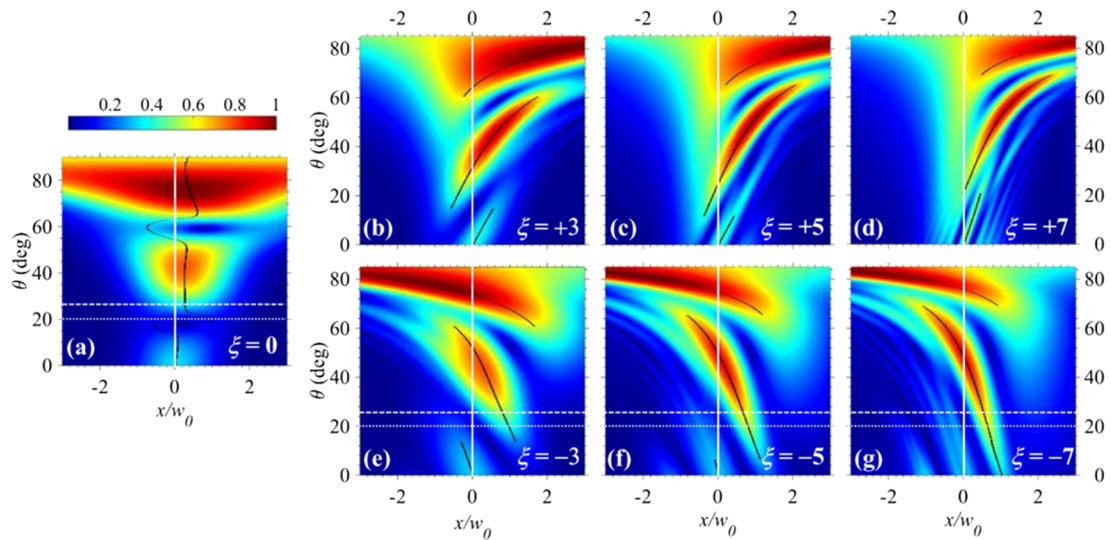
Fig. 3. Distribution of the normalized modulus $|E_y^{(r)}/E_0|$ of the reflected field at the upper surface of the plate (at $z=0$) as a function of the x coordinate and the incidence angle θ for values of the spatial phase modulation parameter equal to: (a) $\xi=0$, (b) $\xi=+3$, (c) $\xi=+5$, (d) $\xi=+7$, (e) $\xi=-3$, (f) $\xi=-5$, and (g) $\xi=-7$. Black lines follow the position of the absolute maximum of the field amplitude when θ varies. The horizontal dotted and dashed lines in (a), (e), (f), and (g) correspond to incidence angles $\theta=20°$ and $\theta=25°$ and refer to the cases depicted in Fig. 4 and discussed in Section 4. The vertical white lines show the position of the center of the incident beam ($x=0$).
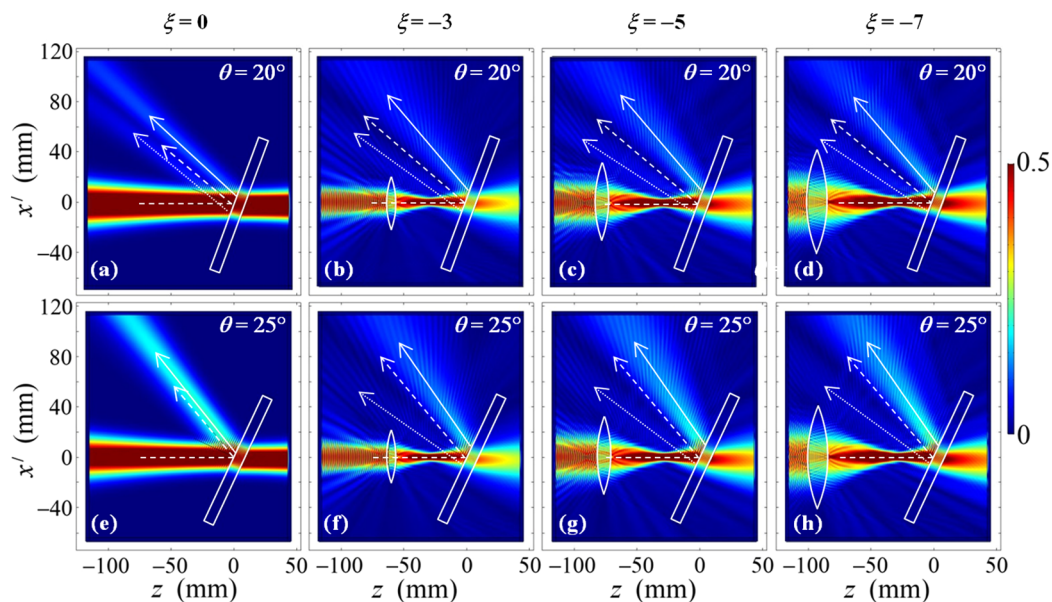

Fig. 4. Numerical simulation of the total electric field amplitude distribution (normalized with respect to E_0) for values of the spatial phase modulation parameter equal to (a), (e) $\xi=0$, (b), (f) $\xi=-3$, (c), (g) $\xi=-5$, and (d), (h) $\xi=-7$, and for incidence angles $\theta=20°$ (top panels) and $\theta=25°$ (bottom panels), in the case where the phase of the incident Gaussian beam is spatially modulated using a parabolically shaped biconvex lens. The white dashed line denotes the center of the incoming beam, and the white dashed arrow indicates the direction of its specular reflection. The solid and dotted arrows show the propagation directions of the first and second reflected beams, respectively. Note that the color scale for the normalized field amplitude has been truncated to the [0; 0.5] interval to enhance the readability of the graphs.

reflected wave. The analytical calculations depicted in Fig. 3 show that, for such incidence angles, an increase of the spatial phase modulation (increase of $|\xi|$) leads to an increase of the lateral beam shift. It can also be noted that for $0 < \theta < 15°$ and $\theta > 20°$, the lateral shift experienced upon reflection by a spatially phase-modulated beam is coupled with significantly larger values of the reflected field than is the case for a non-modulated beam ($\xi=0$). This fact makes spatially phase-modulated beams

particularly useful for so-called weak measurements of lateral beam shifts [7,17,19]. For increasing absolute values of the modulation parameter, however, the reflected beam also experiences an increased reshaping [see Figs. 3(d) and 3(g)], so that a compromise, when choosing the value of the phase modulation parameter, must be found among increased lateral shift, large reflected intensity, and distortion of the beam.

Finally, Fig. 3 also shows that the general tendency for the dependence of the lateral shift on the angle of incidence is that its evolution when θ increases is reversed (although non-symmetrically with respect to $x = 0$) upon a sign reversal of the spatial modulation parameter ξ, as can readily be seen when comparing Figs. 3(b) and 3(e), Figs. 3(c) and 3(f), or Figs. 3(d) and 3(g). However, as should be expected, for incidence angles around normal incidence ($\theta = 0$), calculations show that the distribution of the Gaussian beam field is symmetric with respect to $x = 0$ for any value of ξ.

Overall, the results shown in Fig. 3 clearly highlight the marked sensitivity of the lateral shift of the Gaussian beam upon a spatial modulation of its phase and the way a thoughtful choice of the parameter governing that modulation provides control of both the amplitude and sign of the shift.

It must be noted, however, that the lateral GH beam shift upon reflection is, as mentioned earlier, coupled to an angular shift, also in the plane of incidence, with respect to the purely specular direction, for which the central wave vector of the reflected beam would make the exact same angle θ (in absolute value) with the normal to the surface as the central wave vector of the incoming beam. In reality, the reflection of the beam departs from this simple behavior familiar to ray optics, and an angular shift $\Delta\theta$ is indeed observed that can, in some cases, reach several degrees and thus cannot be neglected, as it must be taken into account for the design of any device exploiting the measurement of the GH effect for sensing purposes. The analytical calculations presented in this section do not allow a simple evaluation of $\Delta\theta$. Estimates based on numerical simulations of the propagation of the reflected beam, however, can be carried out and are presented and discussed below.

4. NUMERICAL SIMULATION OF THE PROPAGATION OF THE REFLECTED PHASE-MODULATED GAUSSIAN BEAM

In this section, we show the results of numerical simulations of the production of a phase-modulated Gaussian beam and its propagation after reflection on the dielectric plate. These simulations were carried out using the COMSOL Multiphysics solver.

Several routes can be followed to obtain the transverse spatial phase modulation of the form $\exp(-i\xi x'^2)$ that appears in Eq. (1) in addition to the longitudinal phase term $\exp(-ik_0 n_S z')$ of a conventional Gaussian beam. We propose here two ways of achieving that goal by focusing a non-modulated Gaussian beam: (1) with a lens with one (plano–convex lens) or two (biconvex lens) parabolically shaped surface profile(s) in the $(x'z')$ plane; or (2) with a flat-surfaced thin lamella exhibiting a parabolic gradient of its refractive index also acting as a converging lens (see Appendix A for details). In both cases, the constitutive parameters of the lens were chosen so that it produces a spatially phase-modulated beam with a negative modulation parameter ($\xi < 0$).

Figure 4 shows the results of numerical simulations where a spatial phase modulation is added to an initially non-modulated Gaussian beam when it is focused with a symmetrical biconvex lens whose thickness (in the direction of the z' axis) follows a parabolic dependence as a function of x' [see Eq. (A4) in

Appendix A]. To properly assess the influence of the resulting phase modulation, the position of the lens relative to the plate as well as the waist of the incoming (non-modulated) Gaussian beam were adapted for each value of the resulting negative modulation parameter ξ, in such a way that the focused (phase-modulated) beam keeps the same waist w_0 at the upper surface of the dielectric plate in all cases. Note that the height h of the lens should be significantly larger than the diameter $2w_0$ of the incoming beam to reduce non-paraxial aberrations. Thus, for each value of ξ, the height of the lens must be adapted in addition to its curvature.

In practice, lateral beam shift measurements are easier to realize at relatively small incidence angles. Here we show in Fig. 4 the reflection of the Gaussian beam simulated for two values of the incidence angle: $\theta = 20°$ (top panels) and $\theta = 25°$ (bottom panels). The first of these values is close to the minimum of reflectivity $|\Re|$ of the plate, as discussed above, whereas for the second value, reflection is characterized by both large values of the lateral shift and large values of $|\Re|$. The analytically calculated profiles of the field modulus at the surface of the plate for those angles of incidence correspond to the horizontal dotted and dashed white lines in Fig. 3.

As was predicted by the calculations based on the analytical model described in Section 3, the Gaussian beam undergoes a reshaping of its field profile even when its phase is not spatially modulated [$\xi = 0$, Figs. 4(a) and 4(e)]. As can be seen in all panels of Fig. 4, the reflected intensity is split between two beams as a result of this reshaping, one of which corresponds to a positive lateral shift Δx (solid arrows) with respect to the specular direction (dashed arrows), and the other corresponds to a negative lateral shift Δx (dotted arrows). In what follows, these two beams will be referred to as the *first* and *second* reflected beams, respectively.

At incidence angle $\theta = 20°$ [Figs. 4(b)–4(d)], these two beams are of comparable amplitudes for all values of the modulation parameter ξ (with the first reflected beam corresponding to $\Delta x > 0$ only slightly brighter), but as mentioned above, the overall reflected intensity is low, as this incidence angle coincides with low values of $|\Re|$.

For all intents and purposes, the case where incidence angle θ is equal to $25°$ [Figs. 4(f)–4(h)] is more interesting, since the detection of beam shifts is bound to be easier in this case due to the larger values of reflected intensity. At that incidence angle, the intensities of the two reflected beams greatly differ, with the first beam (solid arrow, for $\Delta x > 0$) much brighter than the second one (dotted arrow, for $\Delta x < 0$), and thus more suitable for potential applications. The position of the center (defined as the location where intensity is maximum) of the first reflected beam at the surface of the plate can be numerically deduced from the simulations, and its comparison with that of the incoming beam yields the positive value of the lateral shift Δx it undergoes. Similarly, the direction of propagation of either first or second reflected beam, obtained through a numerical determination of its center, can be compared to the specular direction, which leads to the value of the angular shift $\Delta\theta = \theta_r - \theta$, where θ_r denotes the absolute value of the angle between the central propagation axis of a reflected beam and the normal to the top surface of the plate. The angular shift thus determined is positive for the first reflected beam, whereas it is

negative for the less bright second reflected beam—meaning that $\theta_r > \theta$ and $\Delta\theta > 0$ for the first reflected beam, and $\theta_r < \theta$ and $\Delta\theta < 0$ for the second one (whereas $\theta_r = \theta$ in the case of specular reflection).

The results of the analytical and numerical determinations of the normalized lateral spatial shift $\Delta x/\lambda_0$ of the brighter first reflected beam are compared in Fig. 5(a) as functions of ξ for $-7 \leq \xi \leq 0$ and for $\theta = 25°$. The error bars are those of the numerical procedure used for the determination of the reflected beam center at the upper surface of the plate ($z = 0$), with an uncertainty related to the reshaping of that beam (as shown in Fig. 3). The values of Δx obtained with both approaches are in a satisfactorily good agreement for all values of ξ considered in our calculations, and for $-3 \leq \xi \leq 0$, indicate a steady increase of the shift (by a factor that can slightly exceed two) when the absolute value of parameter ξ increases, i.e., when the transverse modulation of the phase of the incoming Gaussian electric field increases. For larger values of $|\xi|$ (for $-7 \leq \xi \leq -3$), both methods seem to indicate a general tendency for Δx to decrease slightly. This can be related to the fact that the reshaping undergone by the reflected beam becomes markedly stronger when the modulation parameter increases in absolute value. Thus, for effective control of the enhancement of the lateral shift, one should retain values of the modulation parameter within the interval $-5 \leq \xi \leq -1$. Overall, our calculations show that the lateral shift Δx can exceed twice the value of the wavelength in

vacuum of the incoming beam, that is, reach values of the order of 1 cm.

Similarly, Fig. 5(b) represents the variations of the angular shift $\Delta\theta$ of the first reflected beam for the same incidence angle $\theta = 25°$ and over the same range $-7 \leq \xi \leq 0$ of the phase modulation parameter. Here again, the error bars stem from the procedure used for determination of the central axis of the primary reflected beam. The angular shifts deduced from the numerical simulations are noticeably enhanced when the incoming Gaussian beam is phase modulated (by a factor larger than four when ξ increases from zero to seven in absolute value) and reach several degrees, which makes them easy to detect for potential applications of lateral shift measurements. Note that similar tendencies for lateral and angular shifts can be obtained for the second, much less intense, reflected beam.

As mentioned earlier, similar results can be obtained when the spatial modulation of the Gaussian beam is achieved using a flat-surfaced thin lamella with a spatial gradation of its refractive index $n_{gr}(x')$ obeying a parabolic law along the x' axis. For the case of $\xi < 0$, the refractive index profile of such a thin lamella is described by Eq. (A5) in Appendix A. Again, simulations show a split of the reflected field in two separate beams with different propagation directions (on either side of the specular direction), one being markedly more intense than the other. Figure 6 illustrates this approach with the example of numerical simulations of beam propagation carried out when the refractive index at the center of such a focusing lamella is $n_{gr,c} = n_P$ and for $\xi = -3$. The other parameters are identical to those used in Figs. 3 and 4. In this case, the refractive index in the lamella decreases parabolically along the x' axis from the center of the lamella to its extremities, so that $n_{gr}(x' = \pm H/2) = 1.5$, where $H = 33.4$ mm is the total height of the lamella, whose thickness is chosen as $D = 9.2$ mm. For this set of structural parameters, calculations lead to values of the lateral spatial shift Δx of the first (i.e., brighter) reflected beam, estimated as previously at the surface of the plate coinciding with the (xy) plane,
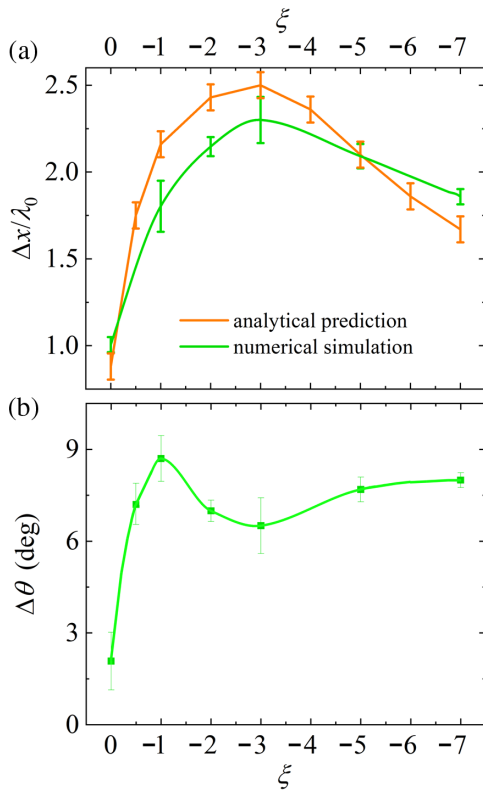
Fig. 5. (a) Comparison of the normalized lateral spatial shift $\Delta x/\lambda_0$ of the first reflected beam as a function of the phase modulation parameter ξ (for $-7 \leq \xi \leq 0$) obtained with the analytical calculation (orange curve) and with the numerical simulation (green curve). (b) Angular shift $\Delta\theta$ of the first reflected beam for the same set of values of ξ obtained using the numerical simulation. The incidence angle is $\theta = 25°$.
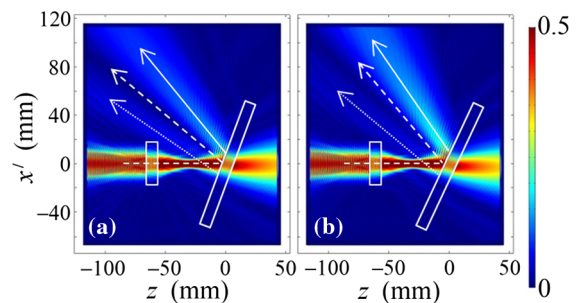
Fig. 6. Numerical simulation of the electric field amplitude distribution (normalized with respect to E_0) for spatial phase modulation parameter $\xi = -3$ and for incidence angles (a) $\theta = 20°$ and (b) $\theta = 25°$ in the case where the phase of the incident Gaussian beam is spatially modulated with the help of a focusing thin lamella with a parabolic refractive index gradient. The white dashed line denotes the central axis of the incoming beam and the normal to the surfaces of the focusing lamella. The white dashed arrow indicates the direction of specular reflection, and the solid and dotted arrows show the central axes of the first (brighter) and second reflected beams, respectively. As in Fig. 4, the color scale for the normalized field amplitude has been truncated to the $[0; 0.5]$ interval to enhance the readability of the graphs.

approximately equal to 2.82 λ_0 for incidence angle $\theta = 20°$ and 2.33 λ_0 for $\theta = 25°$, which is in a good agreement with the corresponding values estimated with a parabolic lens.

5. CONCLUSION

We have shown theoretically and numerically that a spatial transverse modulation of the phase of a Gaussian beam provides a way to control the amplitude and direction of the lateral GH shift to which the reflected beam is subjected with respect to the conventional specular reflection geometry of geometrical optics. We show in Appendix A how, in practice, such a modulation can be achieved by placing a parabolic lens, or a dielectric lamella with a parabolic gradient of its refractive index distribution, in front of a usual Gaussian beam.

Our theoretical analysis and numerical simulations show that the spatial lateral shift of the reflected beam is of the order of one wavelength of the incoming non-modulated Gaussian beam, and that it can be increased up to 2.5 times by introducing a spatial modulation to the beam. For the chosen waist of the microwave beam used for calculations, this translates into an exaltation of the spatial shift from 2.9 to 7.3 mm, which would facilitate its detection in the context of practical applications.

Our numerical simulations of beam propagation indicate that the angular shift that typically accompanies the lateral GH shift in the plane of incidence is also sensitive to the modulation of the phase of the beam. Specifically, we have shown that the angular shift can be increased more than four times by the phase modulation of the Gaussian beam and can reach up to 9°, which, again, makes the measurement of such a shift easier.

We have established the optimal range $[-5, -1]$ of values of the dimensionless parameter ξ that governs the spatial phase modulation for which the lateral shift of the reflected beam is significantly larger than that of a non-modulated beam, but also coincides with large values of the reflection coefficient, while the reshaping of the reflected beam remains limited and thus does not prevent practical application of beam shift measurements.

Such applications can, for example, be found in the microwave domain, where our calculations have shown that the lateral shift of the reflected beam, enhanced and controlled by a well-chosen phase modulation, can reach up to several millimeters, and its experimental measurement in devices such as sensitive sensors, routers, or de/multiplexers is thus facilitated.

It should be noted that the conclusions presented here remain valid for other spectral ranges, for instance, in the visible and near-infrared domains. However, the required precision of the techniques used for the detection of spatial and angular beam shifts in those domains would be higher.

APPENDIX A: OBTAINING A SPATIALLY PHASE-MODULATED GAUSSIAN BEAM

We discuss here two ways of achieving a transverse spatial phase modulation of the electric field of a Gaussian beam of the form $\exp(-i\xi x'^2/w_0^2)$, as indicated in Eq. (1).

The first way consists of focusing a conventional (i.e., without phase modulation) Gaussian beam with a non-spherical lens tailored to yield the required phase modulation. Let us consider such a lens, made of a transparent material with refractive index
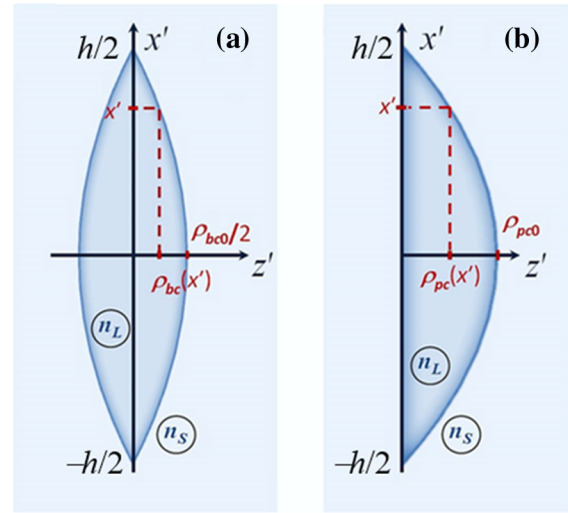

Fig. 7. Schematic of (a) biconvex lens and (b) plano–convex lens with a parabolic thickness profile, height h, and refractive index n_L surrounded by a medium with refractive index n_S. Note that the actual origin of the $(x'y'z')$ Cartesian system of axes is the same as in Fig. 1.

n_L and immersed in a homogeneous medium with refractive index n_S (with $n_S < n_L$, which is the case when the surrounding medium is vacuum or air). Its optical axis coincides with the z' axis (central axis of the incoming beam; see Fig. 1), i.e., the incoming conventional Gaussian beam is incident along the optical axis of the lens. The lens is located close to the waist of the beam, and can thus be considered collimated and its wavefront a plane across the lens, provided the latter's thickness is at all points much smaller than the Rayleigh length z'_R of the beam.

Let us first consider the case of a symmetrical biconvex lens [Fig. 7(a)], introduce the function $\rho_{bc}(x')$ describing the lens thickness profile, and denote $\rho_{bc0} = 2\rho_{bc}(0)$ its total thickness on the optical axis. In the paraxial approximation, the additional transverse spatial phase modulation introduced by the lens verifies

$$\frac{\xi}{w_0^2} x'^2 + 2m\pi = 2k_0(n_L - n_S)\rho_{bc}(x'), \quad m \in \mathbb{Z}. \quad \text{(A1)}$$

As a result, the dependence of ρ_{bc} on the distance x' from the optical axis is thus parabolic (for $-h/2 \leq x' \leq h/2$, where h is the height of the lens), with

$$\rho_{bc}(x') = \frac{\xi x'^2 + 2m\pi w_0^2}{4\pi(n_L - n_S)w_0^2}\,\lambda_0 = \frac{\lambda_0}{4\pi(n_L - n_S)w_0^2}\,\xi x'^2 + \frac{\rho_{bc0}}{2}. \quad \text{(A2)}$$

For $\xi < 0$, the lens is at its thickest at its center, and it is thus converging. The numerical simulations discussed in Section 4 (Figs. 4 and 5) were carried out for such a symmetrical biconvex lens, made of the same fused quartz as the dielectric plate ($n_L = n_P$) and surrounded with air ($n_S = 1$) as well.

Of course, other types of converging lenses can be considered to obtain the required phase modulation, for instance, a plano–convex lens [Fig. 7(b)]. Now the lens profile function, denoted $\rho_{pc}(x')$, verifies, in the paraxial approximation,

$$\frac{\xi}{w_0^2} x'^2 + 2m\pi = k_0(n_L - n_S)\rho_{pc}(x'), \quad m \in \mathbb{Z}, \quad \text{(A3)}$$
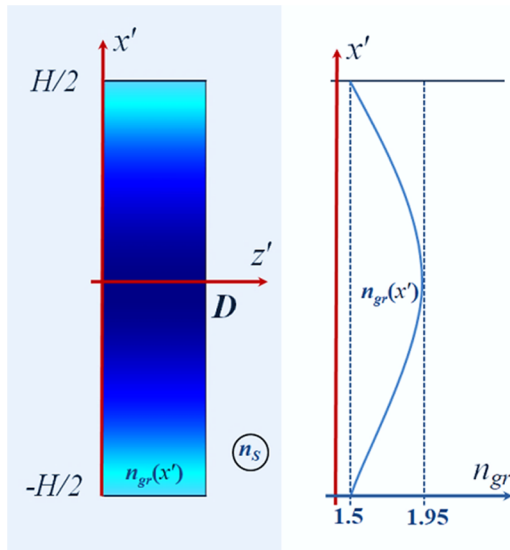
Fig. 8. Schematic of a flat dielectric lamella [thickness D, height H, and parabolic gradient $n_{\mathrm{gr}}(x')$ of its refractive index] acting as a converging lens and surrounded by a medium with refractive index n_S. The color variations inside the lamella schematically illustrate the change in the refractive index along the x' axis.

which, for $-h/2 \le x' \le h/2$, yields

$$\rho_{pc}\left(x'\right) = \frac{\xi x'^2 + 2m\pi w_0^2}{2\pi\left(n_L - n_S\right)w_0^2}\lambda_0 = \frac{\lambda_0}{2\pi\left(n_L - n_S\right)w_0^2}\xi x'^2 + \rho_{pc0},$$

(A4)

where $\rho_{pc}(0) = \rho_{pc0}$ is the thickness of the lens on its optical axis. Again, for $\xi < 0$, the lens is converging.

Yet another way to achieve the desired spatial modulation of the phase of the incident Gaussian beam is to use a flat dielectric lamella whose refractive index n_{gr} exhibits a parabolic gradient in the direction x' perpendicular to the beam propagation direction z' (Fig. 8). It is assumed that the local refractive index $n_{\mathrm{gr}}(x')$ exceeds the ambient refractive index n_S for all $x' \in [-H/2, H/2]$, where H, the height of the lamella, must be larger than the diameter $2w_0$ of the incoming Gaussian beam.

To induce the desired parabolic phase term in Eq. (1), $n_{\mathrm{gr}}(x')$ must vary as

$$n_{\mathrm{gr}}\left(x'\right) = n_{\mathrm{gr},c} + \frac{\lambda_0}{2\pi w_0^2 D}\xi x'^2,$$

(A5)

where D is the thickness of the lamella, and $n_{\mathrm{gr},c}$ is its refractive index at $x' = 0$. The minimal size of such a graded flat lens along of the x' axis is dependent on the width of the incident Gaussian beam. As can be seen from Eq. (A5), the rate of change $(n_{\mathrm{gr}}(x') - n_{\mathrm{gr},c})/x'^2$ of the local refractive index along the transverse dimension of the lamella is determined by both the beam parameters (λ_0, w_0, ξ) and the lamella thickness D.

For $\xi < 0$ the local refractive index decreases with the distance $|x'|$ from the plane $x' = 0$, which is the plane of symmetry of the lamella. The calculations shown and discussed in Section 4 (see Fig. 6) were made for $n_{\mathrm{gr},c} = n_P = 1.95$, $n_{\mathrm{gr}}(\pm H/2) = 1.5$, $H = 33.4$ mm, and $D = 9.2$ mm.

Such a graded-index flat lens can be obtained for different spectral ranges by using additive manufacturing technologies (3D printing), resulting in the fabrication of a composite material, or of a perforated gradient index lamella that provides the required refractive index gradient [50–54].

Disclosures. The authors declare no conflicts of interest.

Data availability. Data underlying the results presented in this paper are not publicly available at this time but may be obtained from the authors upon reasonable request.

REFERENCES

1. F. Goos and H. Hänchen, "Ein neuer und fundamentaler Versuch zur Totalreflexion," Ann. Phys. **436**, 333–346 (1947).
2. F. I. Fedorov, "To the theory of total reflection," Dokl. Akad. Nauk SSSR **105**, 465–468 (1955) (in Russian).
3. C. Imbert, "Calculation and experimental proof of the transverse shift induced by total internal reflection of a circularly polarized light beam," Phys. Rev. D **5**, 787–796 (1972).
4. K. Y. Bliokh and A. Aiello, "Goos–Hänchen and Imbert–Fedorov beam shifts: an overview," J. Opt. **15**, 14001 (2013).
5. R. P. Riesz and R. Simon, "Reflection of a Gaussian beam from a dielectric slab," J. Opt. Soc. Am. A **2**, 1809–1817 (1985).
6. L. I. Perez, "Reflection and non-specular effects of 2D Gaussian beams in interfaces between isotropic and uniaxial anisotropic media," J. Mod. Opt. **47**, 1645–1658 (2000).
7. G. Jayaswal, G. Mistura, and M. Merano, "Weak measurement of the Goos–Hänchen shift," Opt. Lett. **38**, 1232–1234 (2013).
8. Y. S. Dadoenkova, F. F. L. Bentivegna, N. N. Dadoenkova, I. L. Lyubchanskii, and Y. P. Lee, "Influence of misfit strain on the Goos–Hänchen shift upon reflection from a magnetic plate on a nonmagnetic substrate," J. Opt. Soc. Am. B **33**, 393–404 (2016).
9. A. Aiello and J. P. Woerdman, "Theory of angular Goos-Hänchen shift near Brewster incidence," arXiv:0903.3730v2 [physics.optics] (2009).
10. L. Xie, X. Zhou, X. Qiu, L. Luo, X. Liu, Z. Li, Y. He, J. Du, Z. Zhang, and D. Wang, "Unveiling the spin Hall effect of light in Imbert-Fedorov shift at the Brewster angle with weak measurements," Opt. Express **26**, 22934–22943 (2018).
11. Y. S. Dadoenkova, N. N. Dadoenkova, J. W. Kłos, M. Krawczyk, and I. L. Lyubchanskii, "Goos–Hänchen effect in light transmission through biperiodic photonic-magnonic crystals," Phys. Rev. A **96**, 043804 (2017).
12. K. V. Sreekanth, Q. L. Ouyang, S. Han, K.-T. Yong, and R. Singh, "Giant enhancement in Goos-Hänchen shift at the singular phase of a nanophotonic cavity," Appl. Phys. Lett. **112**, 161109 (2018).
13. O. J. S. Santana and L. E. E. de Araujo, "Direct measurement of the composite Goos–Hänchen shift of an optical beam," Opt. Lett. **43**, 4037–4040 (2018).
14. C. Prajapati, D. Ranganathan, and J. Joseph, "Interferometric method to measure the Goos–Hänchen shift," J. Opt. Soc. Am. A **30**, 741–748 (2013).
15. W. Zhang and Z. Zhang, "Collinear heterodyne interferometer technique for measuring Goos–Hänchen shift," Appl. Opt. **57**, 9346–9350 (2018).
16. J. B. Götte and M. R. Dennis, "Generalized shifts and weak values for polarization components of reflected light beams," New J. Phys. **14**, 073016 (2012).
17. T. Tang, J. Li, L. Luo, J. Shen, C. Li, J. Qin, L. Bi, and J. Hou, "Weak measurement of magneto-optical Goos-Hänchen effect," Opt. Express **27**, 17638–17647 (2019).

18. O. J. S. Santana, S. A. Carvalho, S. De Leo, and L. E. E. de Araujo, "Weak measurement of the composite Goos–Hänchen shift in the critical region," Opt. Lett. **41**, 3884–3887 (2016).

19. O. J. S. Santana and L. E. E. de Araujo, "Weak measurement of the Goos–Hänchen shift of partially coherent light beams," J. Opt. Soc. Am. B **36**, 533–540 (2019).

20. Y. S. Dadoenkova, F. F. L. Bentivegna, V. V. Svetukhin, A. V. Zhukov, R. V. Petrov, and M. I. Bichurin, "Controlling optical beam shifts upon reflection from a magneto-electric liquid-crystal-based system for applications to chemical vapor sensing," Appl. Phys. B **123**, 107 (2017).

21. T. Tang, L. Luo, W. Liu, X. He, and Y. Zhang, "Goos–Hänchen effect in semiconductor metamaterial waveguide and its application as a biosensor," Appl. Phys. B **120**, 497–504 (2015).

22. X. Yin and L. Hesselink, "Goos–Hänchen shift surface plasmon resonance sensor," Appl. Phys. Lett. **89**, 261108 (2006).

23. J. Hou, T. Tang, G. Chen, and H. Yang, "Refractive index detection via magneto-optical Goos-Hänchen effect in multilayer structure containing magnetic plate," Superlattices Microstruct. **120**, 766–770 (2018).

24. Y. S. Dadoenkova, F. F. L. Bentivegna, R. V. Petrov, and M. I. Bichurin, "Thermal dependence of the lateral shift of a light beam reflected from a liquid crystal cell deposited on a magnetic plate," J. Appl. Phys. **123**, 033105 (2018).

25. B. Zhao and L. Gao, "Temperature-dependent Goos-Hänchen shift on the interface of metal/dielectric composites," Opt. Express **17**, 21433–21441 (2009).

26. A. Farmani, A. Mir, and Z. Sharifpour, "Broadly tunable and bidirectional terahertz graphene plasmonic switch based on enhanced Goos-Hänchen effect," Appl. Surf. Sci. **453**, 358–364 (2018).

27. P. Han, X. Chang, W. Li, H. Zhang, A. Huang, and Z. Xiao, "Tunable Goos–Hänchen shift and polarization beam splitting through a cavity containing double ladder energy level system," IEEE Photon. J. **11**, 6101013 (2019).

28. H. Sattari, S. Ebadollahi-Bakhtevar, and M. Sahrai, "Proposal for a 1 × 3 Goos-Hänchen shift-assisted de/multiplexer based on a multilayer structure containing quantum dots," J. Appl. Phys. **120**, 133102 (2016).

29. L. Luo, T. Tang, J. Shen, and C. Li, "Electro-optic and magneto-optic modulations of Goos-Hänchen effect in double graphene coating waveguide with sensing applications," J. Magn. Magn. Mater. **491**, 165524 (2019).

30. D. Xu, S. He, J. Zhou, S. Chen, S. Wen, and H. Luo, "Goos–Hänchen effect enabled optical differential operation and image edge detection," Appl. Phys. Lett. **116**, 211103 (2020).

31. Y. S. Dadoenkova, F. F. L. Bentivegna, N. N. Dadoenkova, R. V. Petrov, I. L. Lyubchanskii, and M. I. Bichurin, "Controlling the Goos-Hänchen shift with external electric and magnetic fields in an electro-optic/magneto-electric heterostructure," J. Appl. Phys. **119**, 203101 (2016).

32. R. Macêdo, R. L. Stamps, and T. Dumelow, "Spin canting induced nonreciprocal Goos-Hänchen shifts," Opt. Express **22**, 28467–28478 (2014).

33. T. Tang, J. Qin, J. Xie, L. Deng, and L. Bi, "Magneto-optical Goos-Hänchen effect in a prism-waveguide coupling structure," Opt. Express **22**, 27042–27055 (2014).

34. H. Wu, Q. Luo, H. Chen, Y. Han, X. Yu, and S. Liu, "Magnetically controllable nonreciprocal Goos–Hänchen shift supported by a magnetic plasmonic gradient metasurface," Phys. Rev. A **99**, 033820 (2019).

35. H. Ma and R.-X. Wu, "Nonreciprocal normal-incidence lateral shift for transmitted wave beams through the magnetic photonic crystal slab," Appl. Phys. Lett. **116**, 071104 (2020).

36. W. Yu, H. Sun, and L. Gao, "Magnetic control of Goos-Hänchen shifts in a yttrium-iron-garnet plate," Sci. Rep. **7**, 45866 (2017).

37. H. F. Wang, Z. X. Zhou, H. Tian, D. J. Liu, and Y. Q. Shen, "Electric control of enhanced lateral shift owing to surface plasmon resonance in Kretschmann configuration with an electro-optic crystal," J. Opt. **12**, 045708 (2010).

38. A. Madani and S. R. Entezar, "Tunable enhanced Goos-Hänchen shift in one-dimensional photonic crystals containing graphene monolayers," Superlattices Microstruct. **86**, 105–110 (2015).

39. X. Jiao, Z. Wang, and Y. Cai, "Goos-Hänchen shift in single crystal silicon induced by the electro-optic effects," Phys. Stat. Solidi B **256**, 1900188 (2019).

40. A. A. Zharov, N. A. Zharova, and A. A. Zharov, Jr., "Phase control of the giant resonant Goos–Hänchen shift," JETP Lett. **112**, 65–70 (2020).

41. W. Nasalski, "Modified reflectance and geometrical deformations of Gaussian beams reflected at a dielectric interface," J. Opt. Soc. Am. A **6**, 1447–1454 (1989).

42. Yu. F. Nasedkina and D. I. Sementsov, "Longitudinal shift and transformation of a Gaussian beam upon reflection from a thin plate," Opt. Spectrosc. **102**, 777–784 (2007).

43. Yu. F. Nasedkina, D. I. Sementsov, and O. V. Mosin, "Modification of Gaussian beams reflected by a thin amplifying plate," J. Commun. Technol. Electron. **53**, 1391–1398 (2008).

44. V. B. Yurchenko, M. Ciydem, M. L. Gradziel, and J. A. Murphy, "Major reshaping of narrow beams by resonant multilayer structures," Opt. Express **28**, 8211–8222 (2020).

45. P. Xiao, "Beam reshaping in the occurrence of the Goos–Hänchen shift," J. Opt. Soc. Am. B **28**, 1895–1898 (2011).

46. K. N. Pichugin, D. N. Maksimov, and A. F. Sadreev, "Goos–Hänchen and Imbert–Fedorov shifts of higher-order Laguerre–Gaussian beams reflected from a dielectric slab," J. Opt. Soc. Am. A **35**, 1324–1329 (2018).

47. G. P. Agrawal, *Nonlinear Fiber Optics* (Academic, 2019).

48. Yu. S. Kivshar and G. P. Agrawal, *Optical Solitons* (Academic, 2003).

49. M. Born and E. Wolf, *Principles of Optics* (Cambridge University, 1999).

50. A. Camposeo, L. Persano, M. Farsari, and D. Pisignano, "Additive manufacturing: Applications and directions in photonics and optoelectronics," Adv. Opt. Mater. **7**, 1800419 (2019).

51. Y. Wu, P. S. Grant, and D. Isakov, "3D-printed λ/4 phase plate for broadband microwave applications," Opt. Express **26**, 29068–29073 (2018).

52. A. Petosa and A. Ittipiboon, "Design and performance of a perforated dielectric Fresnel lens," IEE Proc. Microw. Antennas Propag. **150**, 309–314 (2003).

53. S. Zhang, "Design and fabrication of 3D-printed planar Fresnel zone plate lens," Electron. Lett. **52**, 833–835 (2016).

54. A. P. Haring, A. U. Khan, G. Liu, and B. N. Johnson, "3D printed functionally graded plasmonic constructs," Adv. Opt. Mater. **5**, 1700367 (2017).